Progress In Electromagnetics Research C, Vol. 138, 13–26, 2023

Multi-Objective Optimization and Analysis of a Novel Permanent Magnet Synchronous Motor

Huajun Ran, Linfeng Wu*, Wenbo Bai, Junye Zhao, and Yunpan Liu

Abstract—In order to reduce the cogging torque and improve the back electromotive force (EMF) performance of the motor, a three-phase permanent magnet (PM) synchronous motor with magnetic pole eccentricity and slotting design is proposed in this paper. Firstly, the analytical expression for the cogging torque of the motor is derived based on the energy method, and the factors influencing cogging torque are analyzed. Subsequently, taking the cogging torque and the amplitude of the back EMF as the optimization objectives, the response surface method (RSM) and multi-objective genetic algorithm (MOGA) are combined to obtain the optimal values for the eccentricity distance of the PMs, slotting radius, and slot position. Finally, a finite element model is established for simulation comparison. The results show that compared with the traditional model, the optimized model effectively reduces the cogging torque while slightly sacrificing the back-EMF amplitude, and improves the sine degree of the no-load back-EMF.

1. INTRODUCTION

Permanent magnet (PM) motors are extensively utilized in industrial sectors like aerospace and electric vehicles due to their numerous advantages over traditional electric excitation motors. These advantages include enhanced efficiency, energy conservation, superior performance, and light weight [1, 2]. However, PM synchronous motors encounter an issue known as cogging torque, which can cause significant vibration and noise during motor operation [3, 4]. This limitation restricts their application in high-precision systems. Therefore, reducing the cogging torque of the motor has become a crucial area of research in the field of PM synchronous motors.

At present, scholars mainly suppress the cogging torque by changing the topology of the motor. In [5], the optimal step deflection method for reducing the cogging torque of PM motors is proposed. The cogging torque is reduced by gradually deflecting the rotor with the optimal deflection angle or using an unequal step deflection method. In [6], an innovative surface-mounted permanent magnet motor is presented, employing the exact subdomain model and Maxwell stress tensor principle. To mitigate cogging torque, auxiliary slots are introduced to the stator teeth. The impact of auxiliary slot parameters, such as number, width, and position, on cogging torque is thoroughly investigated. In addition, by improving the structure of the permanent magnet, the cogging torque is effectively reduced by adopting the methods of segmentation, slotting, and changing the pole arc coefficient [7–9]. Moreover, some scholars have taken measures to reduce the cogging torque of the motor in the field of control [10, 11]. Furthermore, numerous researchers have employed the response surface method (RSM) and multi-objective genetic algorithm (MOGA) to optimize the motor's design parameters, thereby enhancing its electromagnetic performance [12, 13]. However, the change of stator slot and PM structure will also affect the amplitude of the back-EMF, thus reducing the torque density of the motor.

Received 12 July 2023, Accepted 6 September 2023, Scheduled 23 September 2023
* Corresponding author: Linfeng Wu (1072442823@qq.com).
The authors are with the College of Electrical Engineering & New Energy, China Three Gorges University, Yichang, China.

In order to reduce the cogging torque without losing large torque performance, a 48-slot 4-pole permanent magnet synchronous motor with PM slotting and magnetic pole offset is proposed in this paper. In Section 2, the analytical expression of the cogging torque of the PM synchronous motor is derived and analyzed. In Section 3, the response surface method is used to establish the mathematical model between the cogging torque and the auxiliary slot parameters, and the optimal auxiliary slot parameters are calculated by GA. In Section 4, a finite element simulation model is established for comparative verification. Finally, some conclusions are drawn in Section 5.

2. TOPOLOGY AND ANALYTICAL CALCULATION OF COGGING TORQUE

2.1. Topology of the Motor

The surface-mounted PM motor is shown in Fig. 1. The traditional model in Fig. 1(a) is a 48-slot-4-pole structure. The proposed model incorporates an eccentric and open auxiliary slot design for the PMs, as illustrated in Fig. 1(b). Specifically, two symmetrical semi-circular auxiliary slots are created on the PMs to achieve the eccentric design. The angle between the center line of the auxiliary slot and the center line of the PM is θ. The auxiliary slot on the next adjacent magnetic pole is offset from the previous magnetic pole to both sides at the same angle γ, and the eccentricity of the PM is h. The important structural parameters of the motor are listed in Table 1.

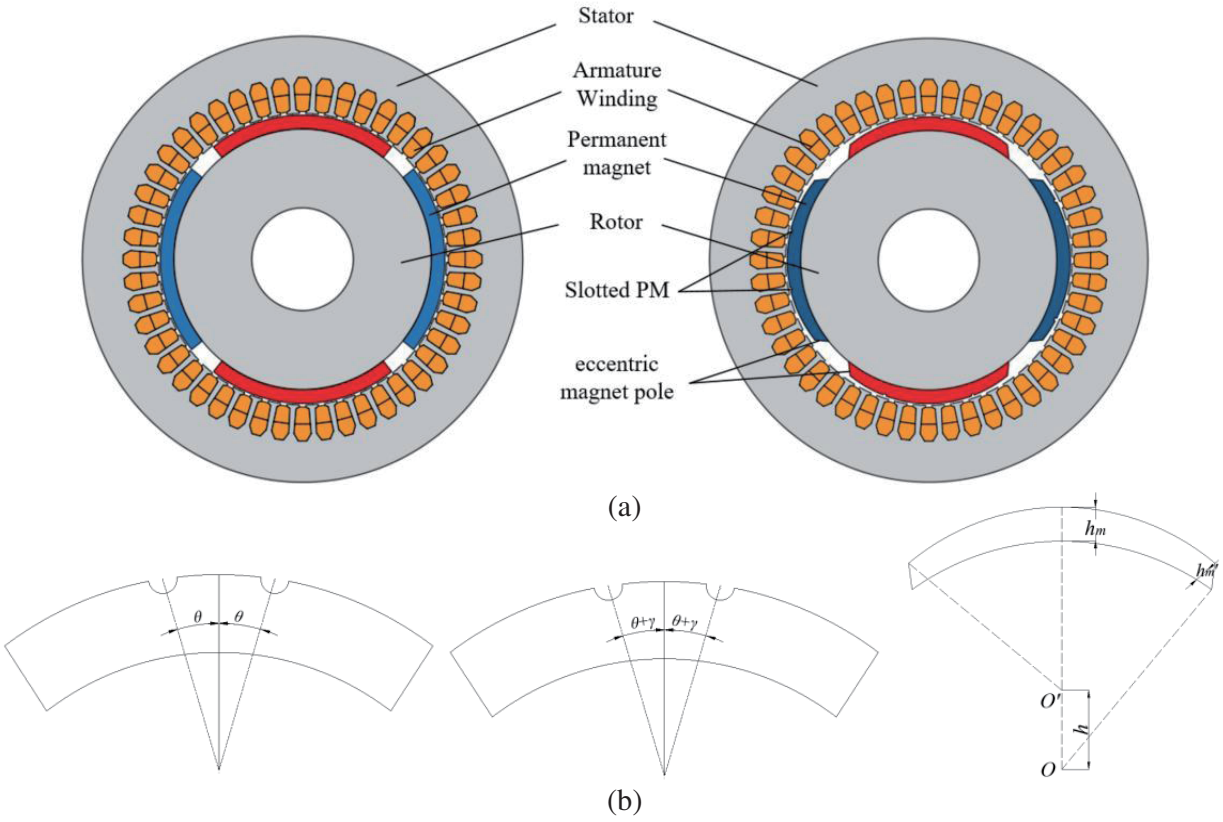

Figure 1. Topology of motors: (a) Traditional and proposed models; (b) Slotting and eccentricity.

2.2. Analytical Calculation of Cogging Torque

The cogging torque (T_{cog}) is defined as the negative rate of change of the motor's magnetic field energy W with respect to the position angle α under the condition that the motor is in an unenergized state.

$$T_{cog} = -\frac{\partial W}{\partial \alpha} \tag{1}$$

Table 1. Structural parameters of the motor.

Parameters	Value
Stator outer radius/mm	65
Rotor outer radius/mm	38
Rotor inner radius/mm	15
length of air gap/mm	0.5
PM embrace	0.8
PM material	NdFeB
Rotation speed/rpm	1500
PM thickness/mm	4
Axial length/mm	145
Rated current (rms)/A	10

If the saturation is neglected and assume infinite magnetic permeability for the armature core, the magnetic field energy can be approximated as equal to the magnetic field energy in the air gap between the motor and the PM. Thus, the magnetic field energy can be expressed as follows:

$$W \approx W_{airgap+PM} = \frac{1}{2\mu_0} \int\limits_V B^2 dV \tag{2}$$

where μ_0 is the air permeability, and the distribution of air gap flux density along the armature surface of PM motor can be approximately written as:

$$B(\theta, \alpha) = B_r(\theta) \frac{h_m(\theta)}{h_m(\theta) + \delta(\theta, \alpha)} \tag{3}$$

where B_r, h_m, and δ are the remanence of PM, the thickness of PM, and the effective air gap length, respectively. Combining Equations (3) and (2), W is expressed as follows:

$$W = \frac{1}{2\mu_0} \int\limits_V B_r^2(\theta) \left(\frac{h_m(\theta)}{h_m(\theta) + \delta(\theta, \alpha)} \right)^2 dV \tag{4}$$

By Fourier decomposition of B_r^2 and $\{h_m(\theta)/(h_m(\theta) + \delta(\theta\alpha))\}^2$, respectively, the following formula can be obtained.

$$\begin{cases} B_r^2(\theta) = B_{r0} + \sum\limits_{n=1}^{\infty} B_{rn} \cos 2np\theta \\ \left(\dfrac{h_m(\theta)}{h_m(\theta) + \delta(\theta, \alpha)} \right)^2 = G_0 + \sum\limits_{n=1}^{\infty} G_n \cos nq(\theta + \alpha) \end{cases} \tag{5}$$

$$\begin{cases} B_{r0} = \alpha_p B_r^2 \\ B_{rn} = \dfrac{2}{n\pi} B_r^2 \sin n\alpha_p \pi \end{cases} \quad \begin{cases} G_0 = \left(\dfrac{h_m}{h_m + \delta} \right)^2 \\ G_n = \dfrac{2}{n\pi} \left(\dfrac{h_m}{h_m + \delta} \right)^2 \sin \left(n\pi - \dfrac{nq\theta_{s0}}{2} \right) \end{cases} \tag{6}$$

where α_p is the polar arc coefficient of the PM; p is the pole pairs of the PM; G and G_n are the Fourier decomposition coefficients; q is the number of stator slots; θ_{s0} denotes the radian of the stator slot.

Substituting the obtained formula into Formula (1), the analytical expression of the cogging torque can be obtained as follows:

$$T_{cog(\alpha)} = \frac{qL_{F_e}}{4\mu_0} \left(R_2^2 - R_1^2 \right) \sum_{n=1}^{\infty} nG_n B_{r\frac{nq}{2p}} \sin(nq\alpha) \tag{7}$$

$$B_{r\frac{nq}{2p}} = \frac{4p}{nq\pi} B_r^2 \sin \frac{nq}{2p} \alpha_p \pi \tag{8}$$

where L_{Fe} is the axial length of the armature core, R_1 the outer diameter of the rotor, R_2 the inner diameter of the stator, and n a positive integer. The cogging torque is similar to the induced electromotive force and comprises harmonic components. These components arise from specific air-gap flux density harmonics and can be characterized by corresponding harmonic frequencies f_k:

$$f_k = \frac{k \cdot LCM(2p, q)}{2p}, \quad k = 1, 2, 3, \ldots \tag{9}$$

where $LCM(2p, q)$ is the least common multiple of the number of q and poles $2p$. When $k = 1$, the lowest harmonic frequency is $(LCM(2p, q))/2p$.

According to the above formula, in a surface-mounted PM synchronous motor, increasing the effective air gap length can be achieved by slotting the pole surfaces of the PM and designing the eccentricity. At the same time, the appropriate parameter values of h, r, and γ are selected to achieve the effect of reducing the cogging torque.

3. OPTIMIZATION DESIGN OF MOTOR

3.1. Structural Parameters and Optimization Process

Based on the finite element method (FEM), the parametric model of PM synchronous motor is established. On the basis of determining the optimization objectives and optimization variables, the range of optimization variables is determined by single parameter scanning. Then, the proposed model is optimized based on RSM and MOGA, and the candidate points are obtained. Finally, the correctness of the candidate points is verified in the two-dimensional finite element. The specific optimization process is shown in Fig. 2.

In order to obtain the optimization range of the key design variables of the proposed motor, a parametric model of the motor is built. The specific optimization variables are shown in Fig. 3, which are the height corresponding to the eccentricity of the magnetic pole (h), radius of the auxiliary slot (r), and the increase angle of the adjacent magnetic poles (γ). The initial angle of θ is 6 degrees, and the cogging torque was calculated to be 2.044 N·m.

On this basis, the variables h, r, and γ are scanned by single parameter, as shown in Fig. 4. The effects of hr and γ on T_{cog} and back-EMF are studied, respectively. The T_{cog} fluctuates irregularly with the change of the three parameters, but the amplitude of the back electromotive force fluctuates in a small range with r and γ but decreases greatly with the increase of h. Therefore, in order to lose as little back-EMF amplitude as possible, we reasonably select the optimization range of each parameter, as shown in Table 2.

Table 2. Variable optimization range.

Parameters	Value
h/mm	$0 \sim 9$
r/mm	$0 \sim 1.8$
γ/deg	$2 \sim 10$

3.2. Response Surface Method

During the optimization process of motor parameters, the optimization objective is defined as minimizing the cogging torque and maximizing the back-EMF. In order to obtain the relationship between variables and optimization objectives, this paper obtains accurate optimization values by fitting an analytical formula close to the actual model. The key to establish the analytical formula is to select the sample points required for modeling and establish the response surface model [12]. The formula is expressed as:

$$y = c_0 + \sum_{i=1}^{3} c_i z_i + \sum_{i=1}^{3} c_{ii} z_i^2 + \sum_{i=1}^{2} \sum_{j>i}^{3} z_i z_j + e_r \tag{10}$$

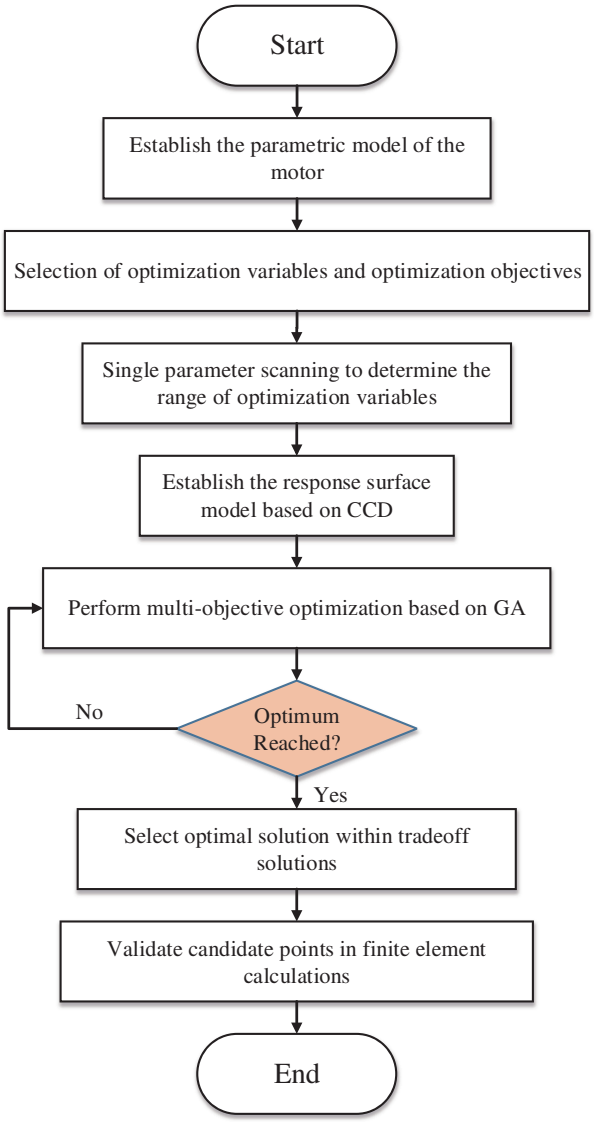

Figure 2. Optimization process of the motor.

where y is the optimization objective, z the optimization variable, c the undetermined coefficient, and e_r the fitting error.

In this paper, the Latin hypercube experimental design CCD (central composite design) sampling method is used to construct the response surface model and generate 14 experimental points. The FEM is employed to calculate the amplitude of T_{cog} and back-EMF at each experimental point, as depicted in Table 3.

The response surface model obtained from the fitted data is depicted in Fig. 5 and Fig. 6. In Fig. 5(a), it is evident that T_{cog} initially decreases with increasing h, followed by an upward trend, while a slight upward trend is observed in T_{cog} as r increases. Fig. 5(b) illustrates that T_{cog} exhibits decreases first and then increases with the increase of γ value, and shows an obvious increasing trend with the increase of r. Furthermore, Fig. 5(c) indicates that T_{cog} follows a pattern of initial decrease and subsequent increase with increasing values of γ and h. In Fig. 6, the response surface model for the three parameters affecting back-EMF is presented. It reveals that the amplitude of back-EMF gradually declines with increasing values of hr and γ. Notably, among these parameters, h has a more significant impact on the amplitude of back-EMF than r and γ. Therefore, in order to achieve the loss of the

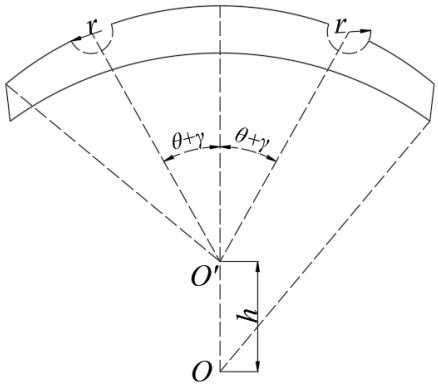

Figure 3. Optimum structure variables.

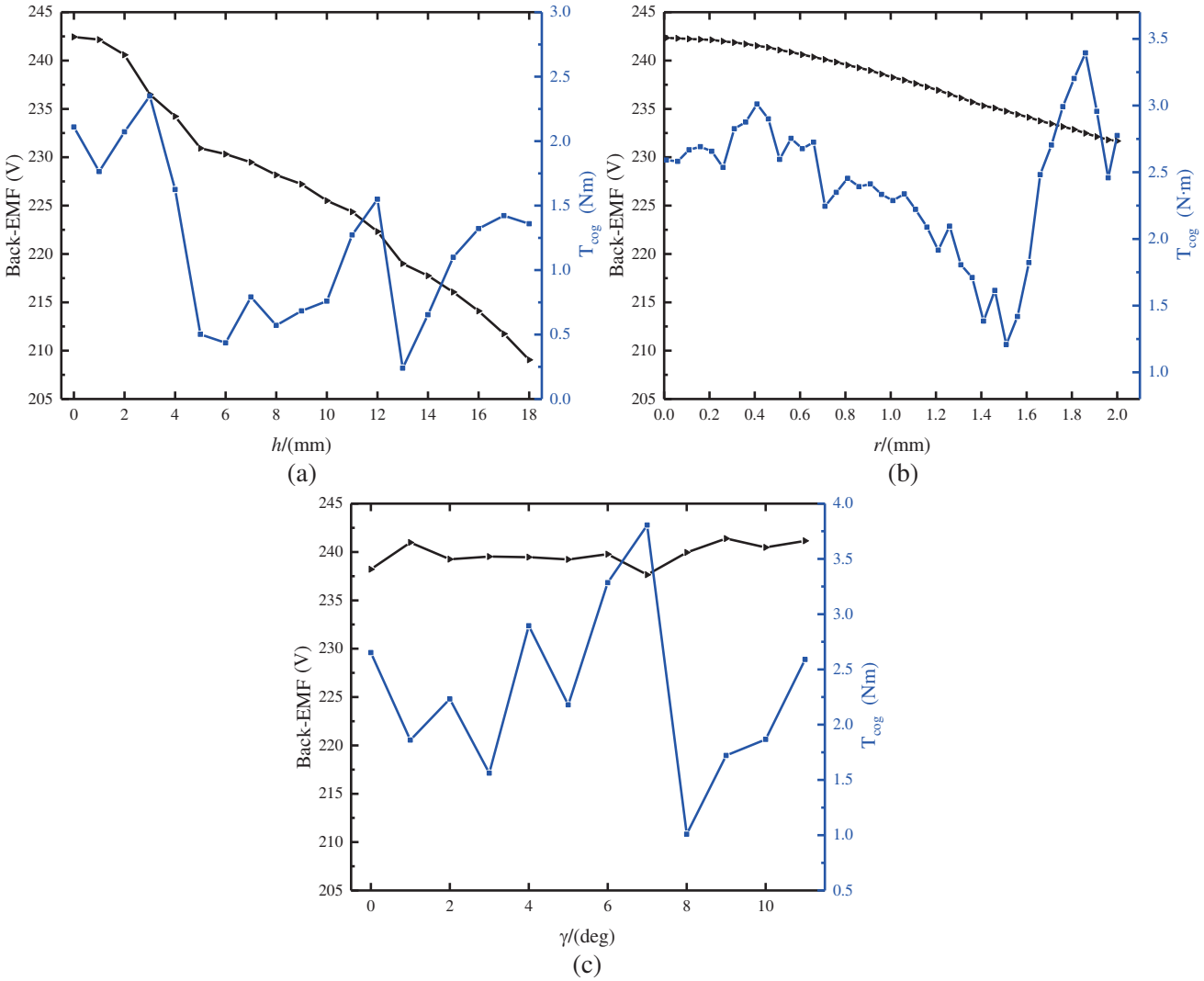

Figure 4. Single parameter scanning results: (a) The effect of h on T_{cog} and Back-EMF; (b) The effect of r on T_{cog} and Back-EMF; (c) The effect of γ on T_{cog} and Back-EMF.

Table 3. Variable optimization range.

Sequence number	h/mm	r/mm	γ/mm	T_{cog}/N·m	*Back-EMF*/V
1	5.9667	1.4033	6.5333	0.88919	229.57
2	7.3667	0.95	7.0667	1.3743	230.34
3	2.2333	1.0633	3.3333	2.5436	240.62
4	6.9	0.15667	9.2	1.68319	233.31
5	2.7	0.3833	3.8667	2.3599	241.46
6	8.7667	0.27	2.8	0.42388	229.94
7	6.4333	1.63	8.667	3.2339	230.8
8	8.3	1.29	8.1333	2.9711	226.95
9	4.1	0.49667	6	1.4673	236.21
10	3.6333	1.1767	9.7333	3.1133	235.65
11	5.0333	0.72333	4.9333	0.80538	233.09
12	3.1667	1.5167	4.4	1.5964	233.14
13	5.5	0.83667	5.4667	0.43868	235.58
14	7.8333	1.7433	2.2667	0.51876	221.31
15	4.5667	0.61	7.6	0.2055	234.89

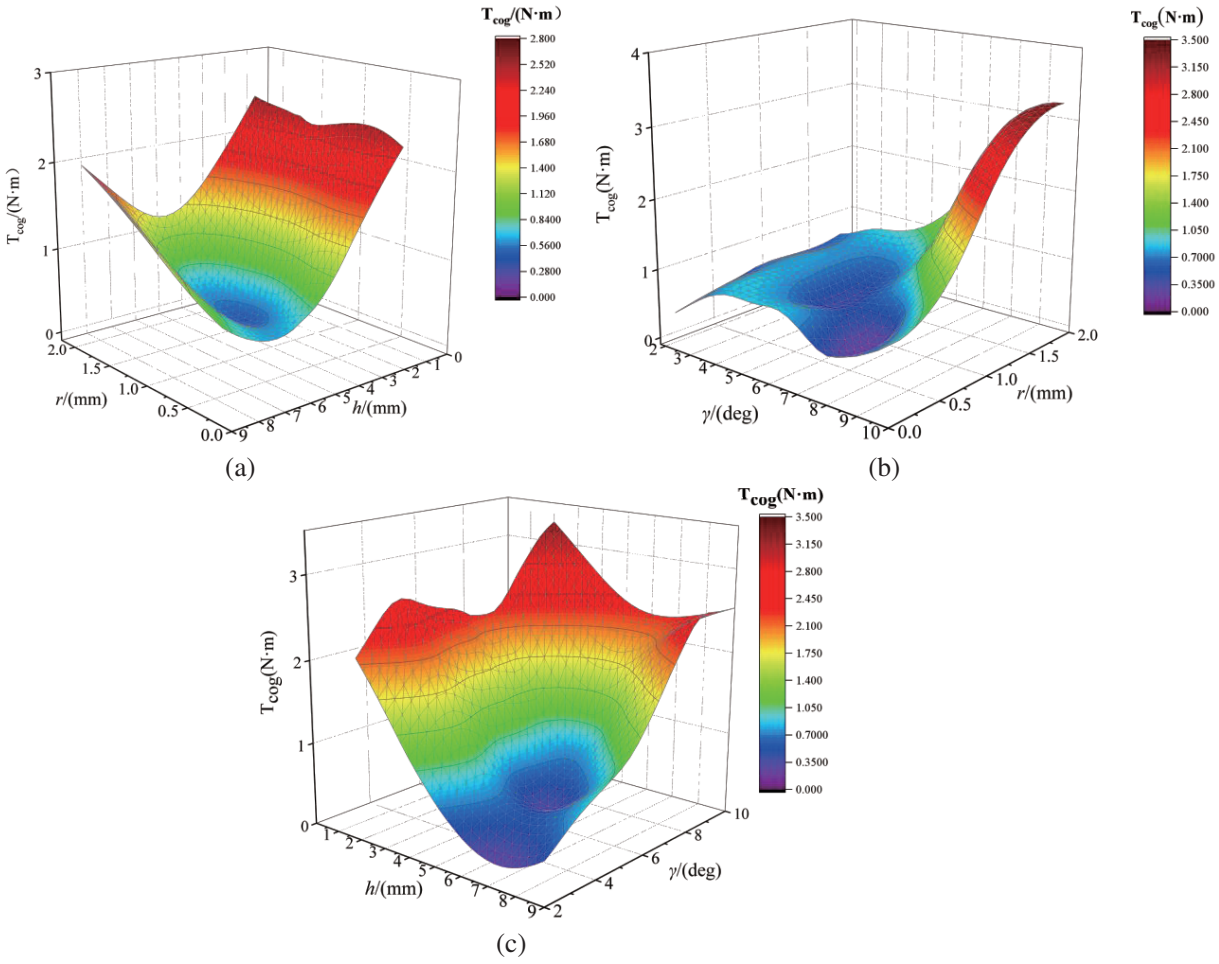

Figure 5. Response surface model: (a) The effect of h and r on T_{cog}; (b) The effect of γ and r on T_{cog}; (c) The effect of$h$ and γ on T_{cog}.

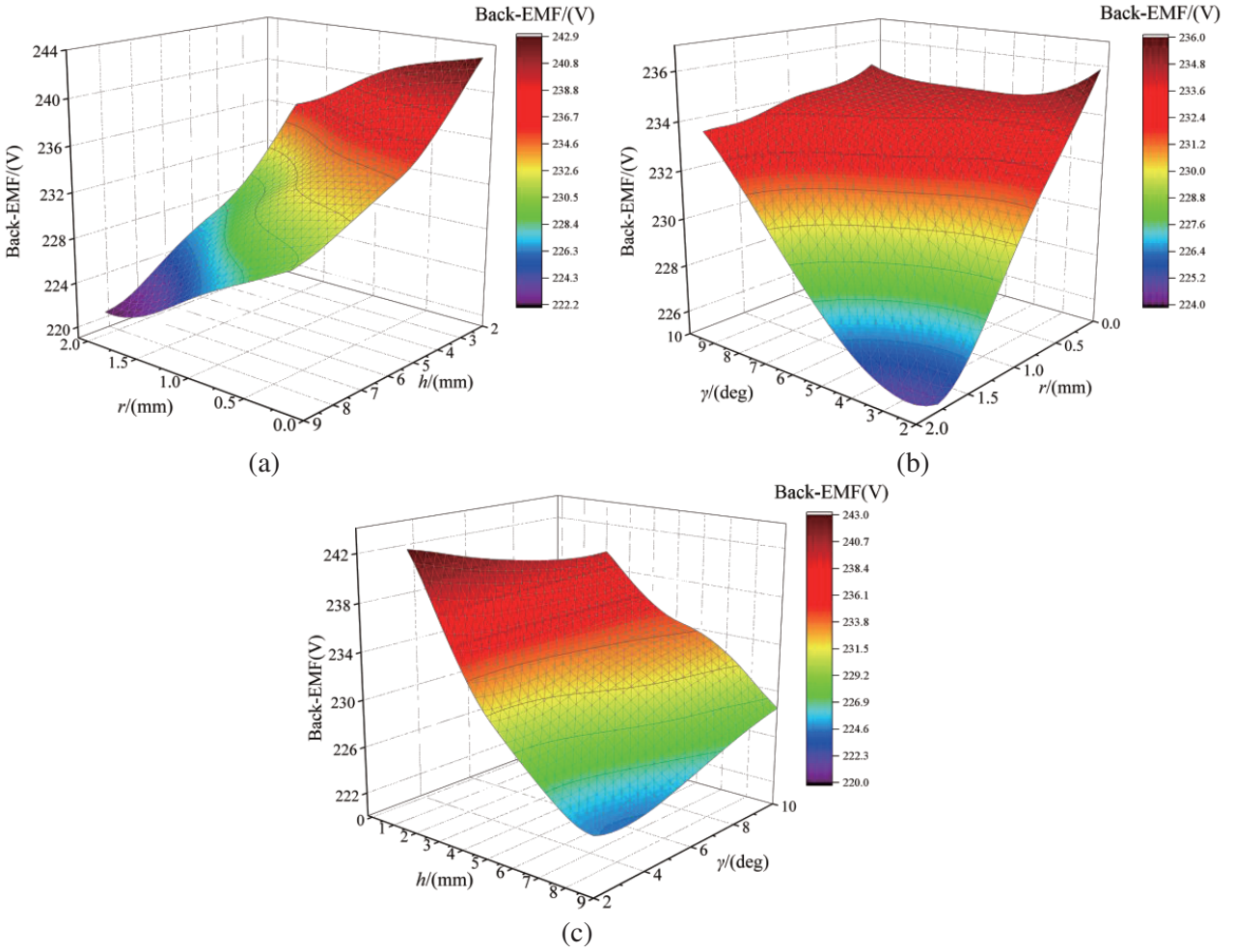

Figure 6. Response surface model: (a) The effect of h and r on back-EMF; (b) The effect of γ and r on back-EMF; (c) The effect of h and γ on back-EMF.

back-EMF amplitude as small as possible, an appropriate parameter value is selected to achieve the effect of reducing the cogging torque.

3.3. Multi-Objective Genetic Algorithm Optimization

The principle of MOGA is mainly based on the global search of each optimization objective function to obtain an initial point that approximates the optimal solution, and then the initial value is used as the original value of the objective optimization function for local solution until an optimal solution is obtained [14]. The objective functions can be written as follows:

$$\begin{cases} \text{Obj} : \begin{cases} \text{Max}(\text{E}(\text{z})) \\ \text{Min}(\text{T}_{\text{cog}}(\text{z})) \end{cases} \\ \text{s.t.} : \quad \text{z}_{\min} < \text{z}_{\text{i}} < \text{z}_{\max} \ \ (\text{i} = 1, 2, 3) \end{cases} \tag{11}$$

where the maximum $E(z)$ and minimum $T_{\text{cog}}(z)$ are the optimization objectives, respectively. The range of the optimization variables (z) is shown in Table 2.

The iterative convergence results of the two optimization objectives are shown in Fig. 7. The maximum back-EMF amplitude and minimum cogging torque amplitude are taken as the target of iterative convergence. After eight iterations, the cogging torque converges to about 0.2 N·m, while the back-EMF amplitude converges to about 230 V.

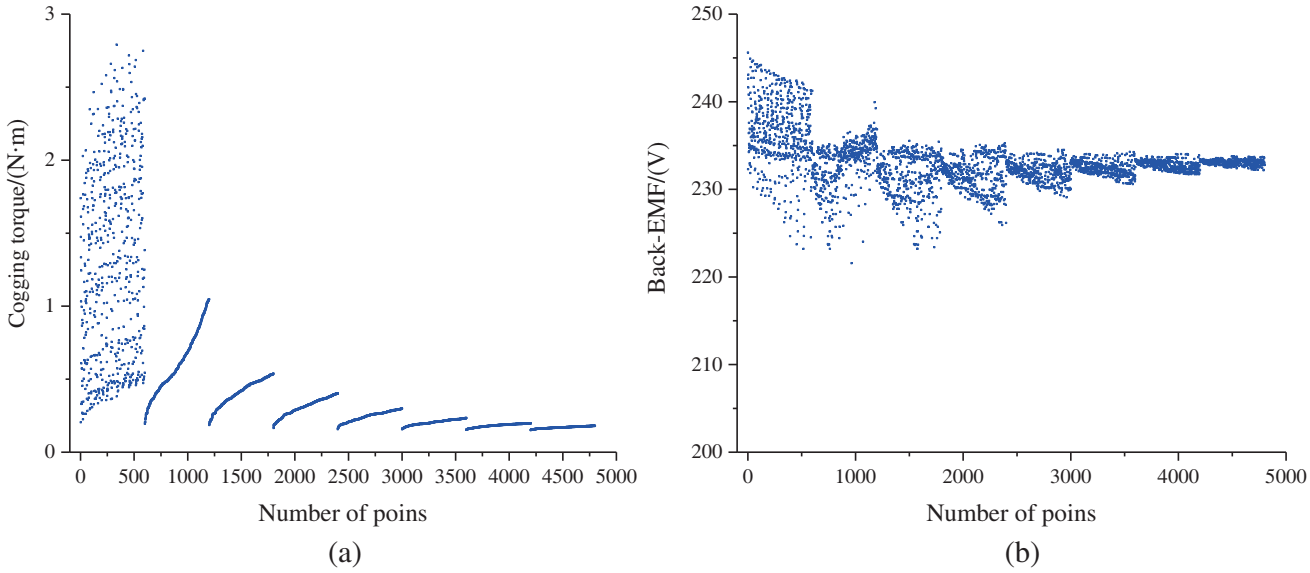

Figure 7. The Iterative convergence of MOGA: (a) cogging torque; (b) back-EMF.

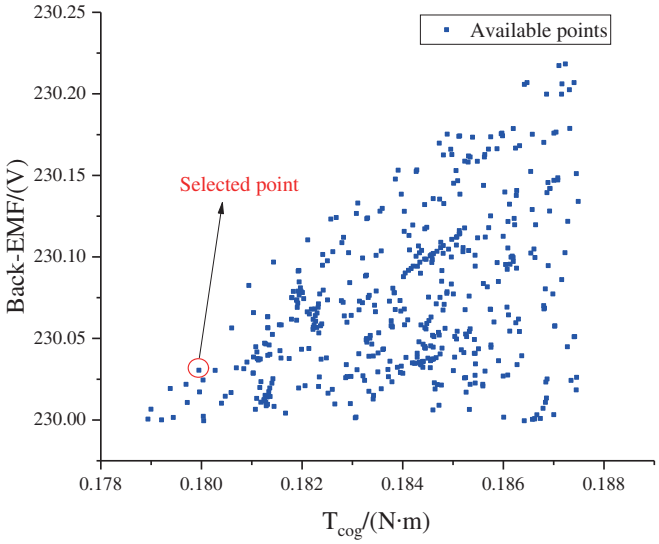

Figure 8. The optimization results of the two optimization objectives.

After iterative convergence, the specific scope of convergence is shown in Fig. 8. The cogging torque of the selected points fluctuates in the range of $0.178\,\mathrm{N\cdot m} \sim 0.188\,\mathrm{N\cdot m}$, and the back-EMF amplitude fluctuates in the range of $230\,\mathrm{V} \sim 230.25\,\mathrm{V}$. The fluctuation range is very small. Therefore, according to the points selected by the red circle, the back-EMF amplitude optimized based on the MOGA algorithm is 230.03 V, and the cogging torque is 0.1789 N·m. The specific values of the corresponding three variables are shown in Table 4.

4. COMPARATIVE ANALYSIS OF ELECTROMAGNETIC PERFORMANCE

To verify the electromagnetic performance of the motor optimized by RSM and MOGA, the traditional and proposed models was established to conduct a comparative analysis, mainly including back-EMF cogging torque, output torque, loss, and efficiency.

Table 4. Variables of optimal design.

Variables	Variation range
h/mm	4.7649
r/mm	0.5088
γ/deg	7.2932

4.1. No-Load Magnetic Field and Back-EMF

Figure 9 shows the magnetic flux density distributions of the traditional and proposed model. The traditional model and the proposed model are not saturated as a whole. It can be seen from Fig. 9(b) that although the thickness of the PM is changed by using the method of eccentricity and slotting, the air gap flux densities in the eccentric region and slotted region are 1.097 T and 0.9603 T, respectively, but there is no risk of saturation. Therefore, the model proposed in this paper will not cause local thermal saturation.

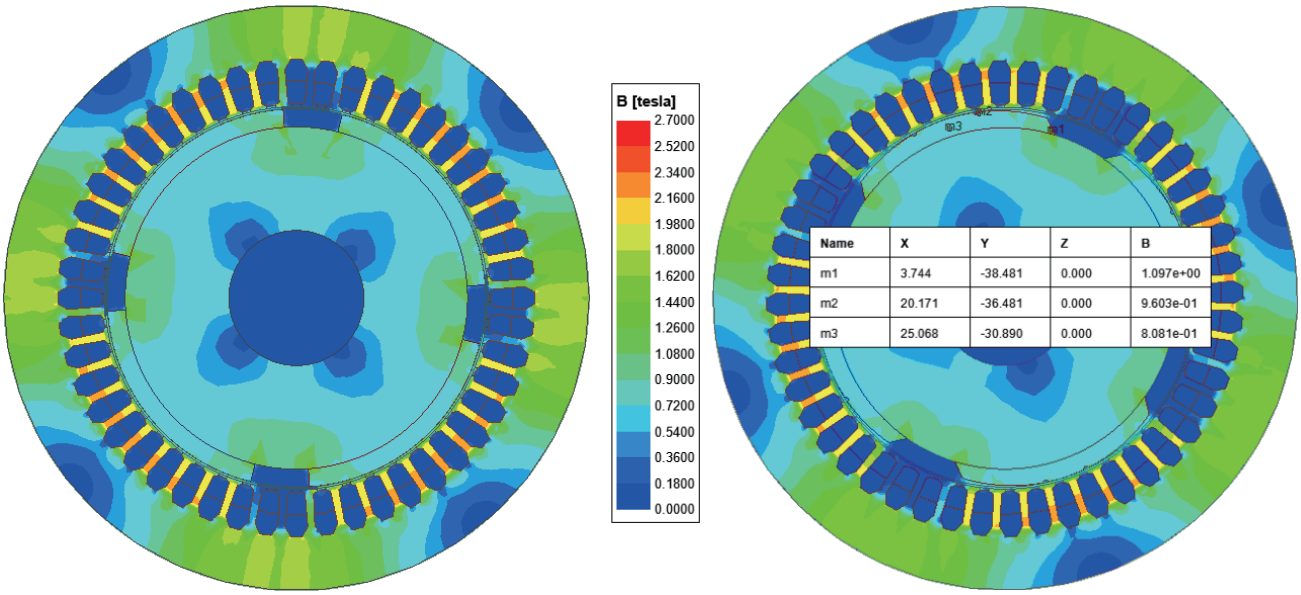

(a) (b)

Figure 9. The magnetic flux density distributions: (a) Traditional; (b) Proposed.

The no-load back-EMF of the motor refers to the reverse EMF generated when the motor has no external load. The influence of the no-load back-EMF on the motor's operation is significant, as it impacts the motor's speed, torque characteristics, and overall efficiency [15]. By measuring and understanding the no-load back-EMF, the performance evaluation and control of the motor can be carried out to achieve more effective motor operation. Taking the A-phase winding as an example, Fig. 10(a) presents the no-load back-EMF waveform comparison between the optimized proposed motor and the traditional motor. The optimized motor exhibits that the amplitude of back-EMF is 229.5 V, which is only 4.9% lower than that of the traditional motor 242.04 V.

The total harmonic distortion (THD) rate reflects the strength of the harmonic components in the back-EMF. The higher the distortion rate is, the more the harmonic components are, and the worse the

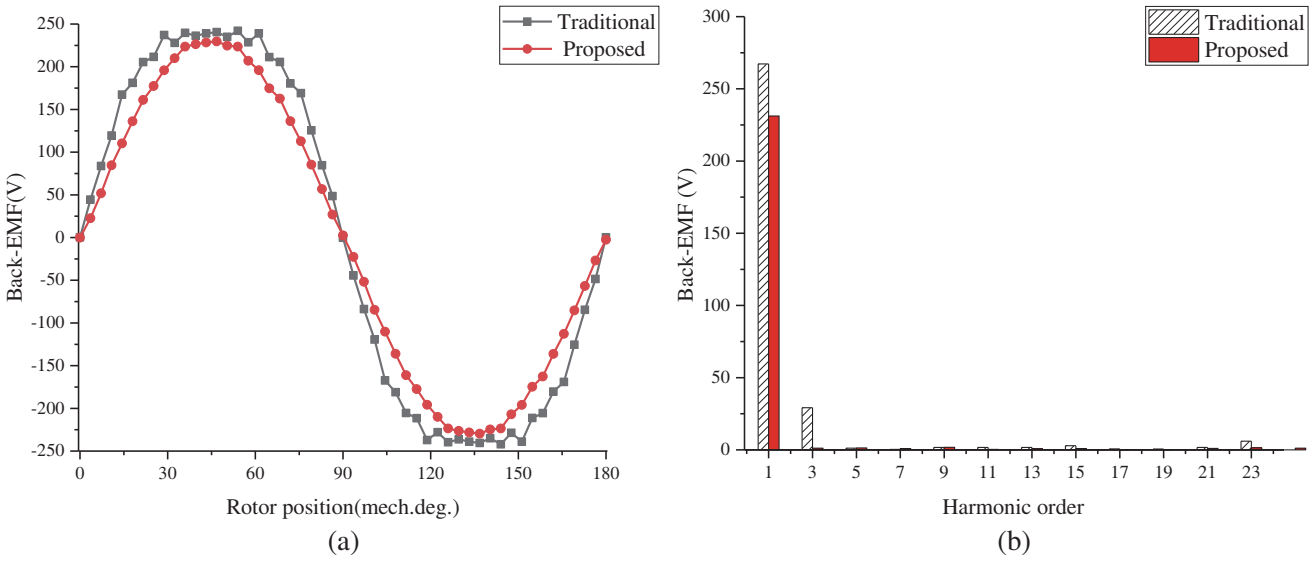

Figure 10. Back-EMF: (a) Waveform; (b) Harmonic distribution.

quality of the back-EMF is. THD can be defined as:

$$\mathrm{THD} = \frac{\sqrt{\sum_{m=2}^{\infty} K_m^2}}{K_1} \times 100\% \tag{12}$$

where K_m is the kth harmonic amplitude, and K_1 is the amplitude of fundamental wave.

Figure 10(b) is the harmonic order diagram of the no-load back-EMF after Fourier decomposition. Although compared with the traditional PM synchronous motor, the fundamental wave content of the proposed motor is reduced, the third harmonic content is greatly reduced, and the sine degree is improved. According to Formula (12), the THD of the proposed motor is reduced from 11.2% to 1.4% compared with the traditional motor, thus improving the reliability and stability of the motor during operation.

4.2. Cogging Torque

The mechanical angle period of the cogging torque of the motor can be calculated to be 7.5°, and the corresponding electrical angle period is 15°. By analyzing the cogging torque waveform depicted in Fig. 11, a distinct disparity in the cogging torque amplitudes between the traditional motor and the proposed motor is evident. The traditional motor exhibits a cogging torque amplitude of 2.044 N·m, and the cogging torque amplitudes of the magnetic pole eccentricity and slotting are 0.408 N·m and 0.638 N·m, respectively. The amplitude of the proposed motor is only 0.172 N·m, which is only 8.4% of the amplitude of the traditional model. Fig. 12 shows the harmonic distribution of traditional and proposed cogging torque waveforms after Fourier decomposition. The proposed design presented in this paper exhibits a notable reduction in the amplitude of each harmonic, thereby effectively minimizing cogging torque. This improvement yields significant enhancements in the motor's overall performance.

4.3. Output Torque

Figure 13 illustrates a comparative torque output curve of the models. The traditional model exhibits the highest output torque, reaching 35.17 N·m. In contrast, the models designed for eccentricity and slotted configurations achieve output torques of 32.57 N·m and 3435 N·m, respectively. After optimization, the proposed model achieves an output torque of 33.73 N·m. Compared with the traditional model, the output torque of the proposed model is only reduced by 4.1%, which is an acceptable result.

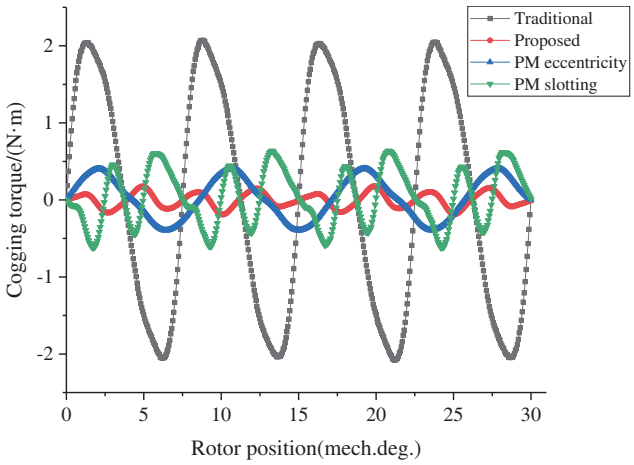

Figure 11. Cogging torque waveform.

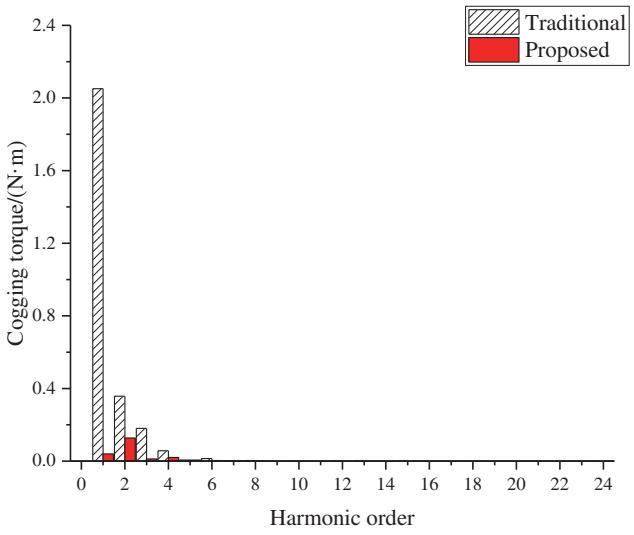

Figure 12. Harmonic distribution of cogging torque.

In terms of torque ripple, the proposed model shows the lowest torque ripple level, which is reduced to 3.48%, while the traditional model shows a large fluctuation of 21.35%. Consequently, with 83.7% reduction of torque ripple, the proposed model can achieve a more stable torque transmission capability.

4.4. Loss and Efficiency

Figure 14 compares the loss of the traditional model and the proposed model. Both models exhibit consistent performance in terms of copper losses. However, due to enhancements made on the PMs, the proposed motor demonstrates superior performance in terms of iron losses and eddy current losses. Detailed loss comparisons are provided in Table 5. Despite a slight reduction in the output power from 5524.08 W to 5297.91 W for the proposed model, its operational efficiency reaches 97.30%, slightly higher than the 97.17% efficiency of the traditional model. This effectively maintains the high-efficiency operational characteristics of the PM synchronous motor.

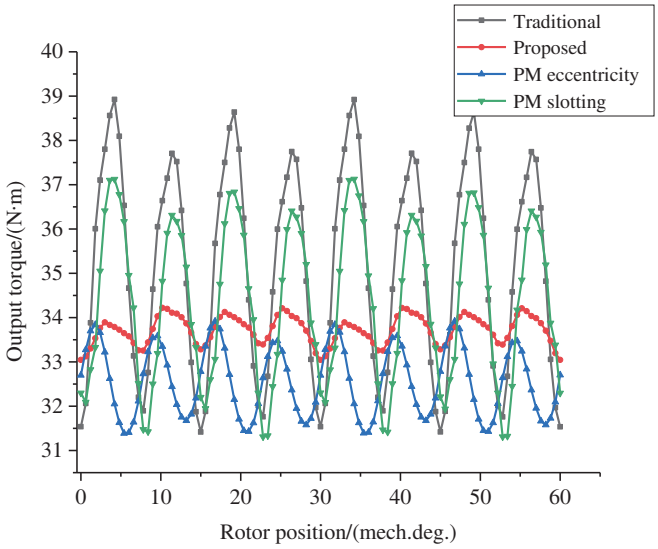

Figure 13. Output torque waveform.

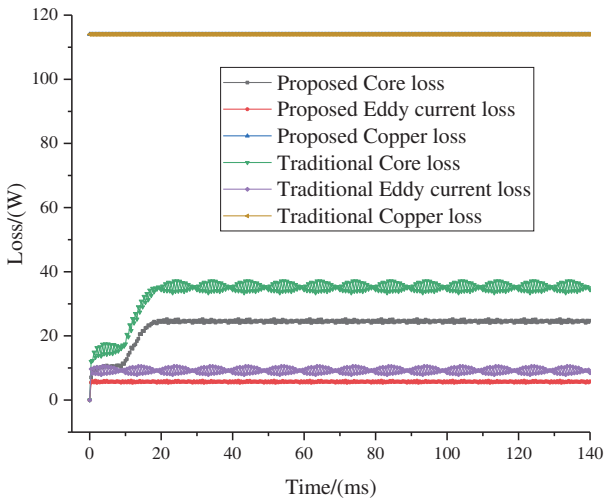

Figure 14. Loss comparison.

Table 5. Various losses, output power and efficiency.

Parameter	Traditional	Proposed
Copper loss (W)	114.01	114.01
Core loss (W)	33.38	23.22
Eddy current loss (W)	9.20	5.68
Total loss (W)	156.59	142.91
Output power (W)	5524.08	5297.91
Efficiency	97.17%	97.30%

5. CONCLUSION

In this paper, a 48-slot 4-pole PM synchronous motor model is constructed to study the influence of PM pole eccentricity and auxiliary slot design on cogging torque. By combining RSM and MOGA, the optimal parameters of PM eccentricity, auxiliary slot radius, and auxiliary slot position are determined to achieve effective reduction of cogging torque. The finite element results show that the electromagnetic performance of the surface-mounted PM synchronous motor can be effectively optimized by using the obtained optimal parameter values. On the premise of only reducing the amplitude of the back-EMF by 4.9%, the reduction of the cogging torque by 91.6% is successfully realized. Therefore, the proposed motor has better performance.

REFERENCES

1. Chen, Y. and B. Liu, "Design and analysis of a five-phase fault-tolerant permanent magnet synchronous motor for aerospace starter-generator system," *IEEE Access*, Vol. 7, 135040–135049, 2019.
2. Jing, L., W. Tang, T. Wang, T. Ben, and R. Qu, "Performance analysis of magnetically geared permanent magnet brushless motor for hybrid electric vehicles," *IEEE Trans. Transp. Electrif.*, Vol. 8, No. 2, 2874–2883, 2022.
3. Si, J., S. Zhao, L. Zhang, R. Cao, and W. Cao, "The characteristics analysis and cogging torque optimization of a surface-interior permanent magnet synchronous motor," *Chinese Journal of Electrical Engineering*, Vol. 4, No. 4, 41–47, 2018.
4. Tong, W., S. Li, X. Pan, S. Wu, and R. Tang, "Analytical model for cogging torque calculation in surface-mounted permanent magnet motors with rotor eccentricity and magnet defects," *IEEE Trans. Energy Convers.*, Vol. 35, No. 4, 2191–2200, 2020.
5. Ge, X., Z. Q. Zhu, G. Kemp, D. Moule, and C. Williams, "Optimal step-skew methods for cogging torque reduction accounting for three-dimensional effect of interior permanent magnet machines," *IEEE Trans. Energy Convers.*, Vol. 32, No. 1, 222–232, 2016.
6. Xia, C., Z. Chen, T. Shi, and H. Wang, "Cogging torque modeling and analyzing for surface-mounted permanent magnet machines with auxiliary slots," *IEEE Trans. Magn.*, Vol. 49, No. 9, 5112–5123, 2013.
7. Lateb, R., N. Takorabet, and F. Meibody-Tabar, "Effect of magnet segmentation on the cogging torque in surface-mounted permanent-magnet motors," *IEEE Trans. Magn.*, Vol. 42, No. 3, 442–445, 2006.
8. Sculler, F., "Magnet shape optimization to reduce pulsating torque for a five-phase permanent-magnet low-speed machine," *IEEE Trans. Magn.*, Vol. 50, No. 4, 1–9, 2013.
9. Chen, Q., H. Shu, and L. Chen, "Simulation analysis of cogging torque of permanent magnet synchronous motor for electric vehicle," *J. Mech. Sci. Technol.*, Vol. 26, 4065–4071, 2012.
10. Lee, G. H., W. C. Choi, S. I. Kim, et al., "Torque ripple minimization control of permanent magnet synchronous motors for EPS applications," *Int. J. Automot. Technol.*, Vol. 12, 291–297, 2011.

11. Hasanien, H. M., "Torque ripple minimization of permanent magnet synchronous motor using digital observer controller," *Energy Conv. Manag.*, Vol. 51, No. 1, 98–104, 2010.
12. Yu, J. and C. Liu, "Multi-objective optimization of a double-stator hybrid-excited flux-switching permanent-magnet machine," *IEEE Trans. Energy Convers.*, Vol. 35, No. 1, 312–323, 2019.
13. Jing, L., W. Liu, W. Tang, and R. Qu, "Design and optimization of coaxial magnetic gear with double-layer PMs and spoke structure for tidal power generation," *IEEE-ASME Trans. Mechatron.*, 2023, doi: 10.1109/TMECH.2023.3261987.
14. Guazzelli, P. R. U., W. C. de Andrade Pereira, C. M. R. de Oliveira, A. G. de Castro, and M. L. de Aguiar, Weighting factors optimization of predictive torque control of induction motor by multi objective genetic algorithm," *IEEE Trans. Power Electron.*, Vol. 34, No. 7, 6628–6638, 2019.
15. Zhang, H., W. Hua, and G. Zhang, "Analysis of back-EMF waveform of a novel outer-rotor-permanent-magnet flux-switching machine," *IEEE Trans. Magn.*, Vol. 53, No. 6, 1–4, 2017.